JOURNAL OF AIRCRAFT
Vol. 47, No. 6, November–December 2010

Declining Angle Effects of the Trailing Edge of a Microramp Vortex Generator

Qin Li* and Chaoqun Liu†
University of Texas at Arlington, Arlington, Texas 76019

DOI: 10.2514/1.C000318

In this paper, the monotone integrated large-eddy simulation method and fifth-order weighted essentially nonoscillatory scheme are used to study the effects of the declining angles of the trailing edge of a microramp vortex generator at $M = 2.5$ and $Re_\theta = 1440$. Two angles are selected for study: 70 and 45°. Results show that the smaller declining angle at $\beta = 45°$ can make the vortices closer to the wall, which is favorable to flow control. However, the improvement in the quality of the boundary layer is less obvious.

Nomenclature

$C_{\text{pitot}_{\text{rc}}}$	=	pitot pressure recovery coefficient
c	=	microramp side length
H_i	=	incompressible boundary-layer shape factor δ^*/θ
h	=	microramp height
M	=	Mach number
p_0	=	pitot pressure
Re_θ	=	Reynolds number based on momentum thickness
x, y, z	=	spanwise, normal, and streamwise coordinate axes
α	=	microramp half-angle
β	=	microramp declining angle of the trailing edge
δ	=	incompressible boundary-layer nominal thickness
δ^*	=	incompressible boundary-layer displacement thickness
θ	=	incompressible boundary-layer momentum thickness

Subscripts

w	=	wall
∞	=	freestream

I. Introduction

RECENTLY, a sub-boundary-layer control device called a micro vortex generator (VG) has received increasing attention by engineers and researchers. In the transonic flow [1,2], it is thought that micro VGs can reduce the shock strength on transonic airfoils in some cases. For the supersonic case, such as with ramp jet engines, it is very important to control the separation flow caused by shock-wave/boundary-layer interaction in order to improve the boundary-layer properties such as the total pressure recovery, shape factor, etc. The conventional bleeding technique [3] has drawbacks such as high drag, compromising intake performance, increasing inlet weight, and mechanical complexity. The micro VG is developed as a new control device that has the benefit of reduced drag and physical simplicity and is considered to be a hopeful substitution for bleeding control. Among the micro VGs, the microramp VG (MVG) seems to be particularly attractive to the intake designer because of its structural robustness [4], while other VGs such as the micro vane have the possibility of breaking away and causing damage to the engine.

Presented as Paper 2010-714 at the 48th AIAA Aerospace Sciences Meeting, Orlando, FL, 4–7 January 2010; received 18 February 2010; accepted for publication 17 July 2010.

*Visiting Postdoctoral Student, Math Department, 411 South Nedderman Drive. Member AIAA.

†Professor, Math Department, 411 South Nedderman Drive. Associate Fellow AIAA.

The basic flow structures in the VG (conventional VG and micro VG) control is thought to produce pairs of counter-rotating streamwise vortices, which are beneficial to separation suppression and improvement of the boundary-layer characteristics. The mechanism of the control is believed to be that the entrainment of streamwise vortices will induce the momentum exchange between the faster outer and slower inner boundary-layer flows. Because the micro VG has the smaller size (approximately 20–40% of the boundary layer), the vortices generated by MVG are found to remain in the boundary layer for a longer streamwise distance than for conventional VGs with the height of the boundary layer [4]. Therefore, how to make the vortices remain in the boundary layer as long as possible becomes one of the key issues in the optimization of micro VGs.

Babinsky et al. [4] conducted experiments on MVG with four different heights from 2 to 6 mm. No fundamental change of the flow structure was observed due to different heights. An empirical relation was discovered between the scaled streamwise distance and the height of vortices, which may be helpful in guiding the flow control. Lee and Loth [5] made a series of computations to investigate a variety of the micro VGs. In addition to varying the size and shape of the micro VG, two hybrid concepts named *thick-vane* and *split-ramp* were tested as well. From their work, a basic mechanism for the lifting up of the vortices was identified as the upwash effect, which comes from the induced vortices interactions with each other. Until now, further research on the influence factors of the flow control has been limited. Apparently, more new investigations are needed.

In this study, the numerical simulation is made on the effect of the declining angle of the trailing edge of the MVG at $M = 2.5$ and $Re_\theta = 1440$. Two angles are selected as 70 and 45°, and the other geometric attributes remain unchanged. Two MVGs are mounted on a flat plate with a long region downstream after the MVG. An approach named monotone integrated large-eddy simulation (MILES) is used, in which the numerical dissipation is used as the subgrid stress model and the well-known fifth-order weighted essentially nonoscillatory (WENO) scheme is applied as the basic numerical scheme. According to the previous work, the result of MILES is in close agreement to that using Smagorinsky's subgrid model [6]. Based on the results of the computation, comparisons are made on the trajectory of vortices and characteristics of the downstream boundary layer.

The paper is arranged as follows: the numerical methods are given in Sec. II; the procedures for grid generation are described in Sec. III; in Sec. IV, large-eddy simulation (LES) results are given for the MVG flow with trailing-edge declining angles of 70 and 45°, and a discussion is made on the LES results; and conclusions are made in Sec. V.

II. Numerical Methods

A. Governing Equations

The governing equations are the nondimensional Navier–Stokes equations in conservative form, described as follows:

$$\frac{\partial Q}{\partial t}+\frac{\partial E}{\partial x}+\frac{\partial F}{\partial y}+\frac{\partial G}{\partial z}=\frac{\partial E_v}{\partial x}+\frac{\partial F_v}{\partial y}+\frac{\partial G_v}{\partial z} \tag{1}$$

where

$$Q=\begin{bmatrix}\rho\\ \rho u\\ \rho v\\ \rho w\\ e\end{bmatrix},\quad E=\begin{bmatrix}\rho u\\ \rho u^2+p\\ \rho uv\\ \rho uw\\ (e+p)u\end{bmatrix},\quad F=\begin{bmatrix}\rho v\\ \rho vu\\ \rho v^2+p\\ \rho vw\\ (e+p)v\end{bmatrix},\quad G=\begin{bmatrix}\rho w\\ \rho wu\\ \rho wv\\ \rho w^2+p\\ (e+p)w\end{bmatrix},\quad E_v=\frac{1}{Re}\begin{bmatrix}0\\ \tau_{xx}\\ \tau_{xy}\\ \tau_{xz}\\ u\tau_{xx}+v\tau_{xy}+w\tau_{xz}+q_x\end{bmatrix}$$

$$F_v=\frac{1}{Re}\begin{bmatrix}0\\ \tau_{yx}\\ \tau_{yy}\\ \tau_{yz}\\ u\tau_{yx}+v\tau_{yy}+w\tau_{yz}+q_y\end{bmatrix},\qquad G_v=\frac{1}{Re}\begin{bmatrix}0\\ \tau_{zx}\\ \tau_{zy}\\ \tau_{zz}\\ u\tau_{zx}+v\tau_{zy}+w\tau_{zz}+q_z\end{bmatrix}$$

$$e=\frac{p}{\gamma-1}+\frac{1}{2}\rho(u^2+v^2+w^2),\qquad q_z=\frac{\mu}{(\gamma-1)M_\infty^2 Pr}\frac{\partial T}{\partial x},\qquad q_y=\frac{\mu}{(\gamma-1)M_\infty^2 Pr}\frac{\partial T}{\partial y},\qquad q_z=\frac{\mu}{(\gamma-1)M_\infty^2 Pr}\frac{\partial T}{\partial z}$$

$$p=\frac{1}{\gamma M_\infty^2}\rho T,\qquad Pr=0.72,\qquad \tau=\mu\begin{bmatrix}\frac{4}{3}\frac{\partial u}{\partial x}-\frac{2}{3}\left(\frac{\partial v}{\partial y}+\frac{\partial w}{\partial z}\right) & \frac{\partial u}{\partial y}+\frac{\partial v}{\partial x} & \frac{\partial u}{\partial z}+\frac{\partial w}{\partial x}\\ \frac{\partial u}{\partial y}+\frac{\partial v}{\partial x} & \frac{4}{3}\frac{\partial v}{\partial y}-\frac{2}{3}\left(\frac{\partial w}{\partial z}+\frac{\partial u}{\partial x}\right) & \frac{\partial v}{\partial z}+\frac{\partial w}{\partial y}\\ \frac{\partial u}{\partial z}+\frac{\partial w}{\partial x} & \frac{\partial v}{\partial z}+\frac{\partial w}{\partial y} & \frac{4}{3}\frac{\partial w}{\partial z}-\frac{2}{3}\left(\frac{\partial u}{\partial x}+\frac{\partial v}{\partial y}\right)\end{bmatrix}$$

The viscous coefficient is given by Sutherland's equation:

$$\mu=T^{\frac{3}{2}}\frac{1+C}{T+C},\qquad C=\frac{110.4}{T_\infty} \tag{2}$$

The nondimensional variables are defined as follows:

$$x=\frac{\tilde{x}}{L},\quad y=\frac{\tilde{y}}{L},\quad z=\frac{\tilde{z}}{L},\quad u=\frac{\tilde{u}}{U_\infty},\quad v=\frac{\tilde{v}}{U_\infty}$$
$$w=\frac{\tilde{w}}{U_\infty},\quad T=\frac{\tilde{T}}{T_\infty},\quad \mu=\frac{\tilde{\mu}}{\mu_\infty},\quad k=\frac{\tilde{k}}{k_\infty}$$
$$\rho=\frac{\tilde{\rho}}{\rho_\infty},\quad p=\frac{\tilde{p}}{\rho_\infty U_\infty^2},\quad e=\frac{\tilde{e}}{\rho_\infty U_\infty^2}$$

where the variables with a tilde are the dimensional counterparts.

Considering the following grid transformation,

$$\begin{cases}\xi=\xi(x,y,z)\\ \eta=\eta(x,y,z)\\ \zeta=\zeta(x,y,z)\end{cases} \tag{3}$$

the Navier–Stokes equations can be transformed to the system in generalized coordinates:

$$\frac{\partial \hat{Q}}{\partial \tau}+\frac{\partial \hat{E}}{\partial \xi}+\frac{\partial \hat{F}}{\partial \eta}+\frac{\partial \hat{G}}{\partial \zeta}=\frac{\partial \hat{E}_v}{\partial \xi}+\frac{\partial \hat{F}_v}{\partial \eta}+\frac{\partial \hat{G}_v}{\partial \zeta} \tag{4}$$

where $\hat{Q}=J^{-1}Q$ and

$$\hat{E}=J^{-1}(\xi_x E+\xi_y F+\xi_z G),\qquad \hat{F}=J^{-1}(\eta_x E+\eta_y F+\eta_z G)$$
$$\hat{G}=J^{-1}(\zeta_x E+\zeta_y F+\zeta_z G),\qquad \hat{E}_v=J^{-1}(\xi_x E_v+\xi_y F_v+\xi_z G_v)$$
$$\hat{F}_v=J^{-1}(\eta_x E_v+\eta_y F_v+\eta_z G_v),\qquad \hat{G}_v=J^{-1}(\zeta_x E_v+\zeta_y F_v+\zeta_z G_v)$$

J^{-1}, ξ_x, etc., are grid metrics, and

$$J^{-1}=\det\left(\frac{\partial(x,y,z)}{\partial(\xi,\eta,\zeta)}\right)$$

$\xi_x=J(y_\eta z_\zeta-z_\eta y_\zeta)$, etc.

B. Finite Difference Schemes and Boundary Conditions

1. *Fifth-Order WENO Scheme for the Convective Terms*

For integrity, the fifth-order WENO [7] scheme will be described as follows. Considering the one-dimensional hyperbolic equation,

$$\frac{\partial u}{\partial t}+\frac{\partial f(u)}{\partial x}=0 \tag{5}$$

the semidiscretized equation can be expressed as follows:

$$\left(\frac{\partial u}{\partial t}\right)_j=-\frac{h_{j+1/2}-h_{j-1/2}}{\Delta x} \tag{6}$$

Considering the positive flux, the three upwind-biased schemes on three basic candidate stencils can be given as

$$\begin{cases}h_1^{+'}=\frac{1}{3}f_{j-2}-\frac{7}{6}f_{j-1}+\frac{11}{6}f_j\\ h_2^{+'}=-\frac{1}{6}f_{j-1}+\frac{1}{3}f_j+\frac{5}{6}f_{j+1}\\ h_3^{+'}=\frac{1}{3}f_j+\frac{5}{6}f_{j+1}-\frac{1}{6}f_{j+2}\end{cases} \tag{7}$$

The superscript + refers to the positive flux after flux splitting. The final nonlinear weighted schemes can be expressed as

$$h_{j+1/2}^{+}=w_1h_1^{+'}+w_2h_2^{+'}+w_3h_3^{+'} \tag{8}$$

where $w_i=b_i/(b_1+b_2+b_3)$, $b_i=\alpha_i/(\varepsilon+IS_i)^2$, $(\alpha_1,\alpha_2,\alpha_3)=(0.1,0.6,0.3)$, and ε is a small quantity to prevent the denominator from being zero, which should be small enough in supersonic problems with shocks (10^{-6}–10^{-10}). IS_i is the smoothness measurement and has the following form:

$$\begin{cases}IS_1=\frac{13}{12}(f_{j-2}-2f_{j-1}+f_j)^2+\frac{1}{4}(f_{j-2}-4f_{j-1}+3f_j)^2\\ IS_2=\frac{13}{12}(f_{j-1}-2f_j+f_{j+1})^2+\frac{1}{4}(f_{j-1}-f_{j+1})^2\\ IS_3=\frac{13}{12}(f_j-2f_{j+1}+f_{j+2})^2+\frac{1}{4}(3f_j-4f_{j+1}+f_{j+2})^2\end{cases} \tag{9}$$

The scheme for $h_{j+1/2}^{-}$ has a symmetric form of $h_{j+1/2}^{+}$ to the point $x_{j+1/2}$.

2. Finite Difference Scheme for the Viscous Terms

Considering the conservative form of the governing equations, the traditional fourth-order central scheme is used twice to compute the second-order viscous terms.

3. Time Scheme

The basic methodology for the temporal terms in Navier–Stokes equations adopts the explicit and third-order total-variation-diminishing type of Runge–Kutta scheme, which can be described as follows [8]:

$$\begin{aligned} u^{(1)} &= u^n + \Delta t L(u^n) \qquad u^{(2)} = \tfrac{3}{4}u^n + \tfrac{1}{4}u^{(1)} + \tfrac{1}{4}\Delta t L(u^{(1)}) \\ u^{n+1} &= \tfrac{1}{3}u^n + \tfrac{2}{3}u^{(2)} + \tfrac{2}{3}\Delta t L(u^{(2)}) \end{aligned} \tag{10}$$

4. Open-Boundary Processing Methods

After analyzing the characteristic relation of the governing equation, an open-boundary condition is presented in [9]. We can take the two-dimensional Euler ($s = 0$) and Navier–Stokes equation ($s = 1$) as example:

$$\frac{\partial \hat{U}}{\partial t} + \frac{\partial \hat{E}}{\partial \xi} + \frac{\partial \hat{F}}{\partial \eta} + s\left(\frac{\partial \hat{E}_v}{\partial \xi} + \frac{\partial \hat{F}_v}{\partial \eta}\right) = 0 \tag{11}$$

Supposing that η corresponds to the grid line heading to the boundary and the propagation direction is corresponding to λ_1, which is one of the characteristic values of *Jacobian* matrix of the flux. For points in the inner field, multiplying Eq. (11) using the left characteristic vector of $\hat{F}$ corresponding to the direction mentioned above, we can get the following equation:

$$\hat{l}_1 \frac{\partial \hat{U}}{\partial t} + \lambda_1 \hat{l}_1 \frac{\partial \hat{U}}{\partial \eta} + \cdots = 0 \tag{12}$$

To eliminate or weaken the reflection from the boundary to the inner field, we present a numerical condition to force the disturbance or reflection from the boundary to the inner field to zero, i.e., to set the velocity of the propagation to zero:

$$\hat{l}_1 \frac{\partial \hat{U}}{\partial t} + \cdots = 0 \tag{13}$$

We can imbed the boundary condition (13) into the governing equation or use the following simplified form of realization [9]:

On boundary $\eta = \eta_{\min}$, no matter whether the flow goes inward or outward, use

$$\frac{\partial \hat{U}}{\partial t} + \frac{\partial \hat{F}^-}{\partial \eta} + \frac{\partial \hat{E}}{\partial \xi} + s\left(\frac{\partial \hat{F}_v}{\partial \eta} + \frac{\partial \hat{E}_v}{\partial \xi}\right) = 0 \tag{14}$$

On the boundary $\eta = \eta_{\max}$, the boundary governing equation can be written as

$$\frac{\partial \hat{U}}{\partial t} + \frac{\partial \hat{F}^+}{\partial \eta} + \frac{\partial \hat{E}}{\partial \xi} + s\left(\frac{\partial \hat{F}_v}{\partial \eta} + \frac{\partial \hat{E}_v}{\partial \xi}\right) = 0 \tag{15}$$

5. Boundary Conditions

The adiabatic zero gradient of pressure and no-slip conditions are used for the wall as

$$\partial T/\partial n = 0, \qquad \partial p/\partial n = 0, \qquad \mathbf{U} = 0 \tag{16}$$

At the upper and outflow boundaries the above open-boundary processing method is used. The boundary condition at the front and back boundary surface in the spanwise direction is assumed to be mirror-symmetric. The reason is based on the assumption that the flow is assumed to be mirror-symmetric within MVG arrays and the computation is only made on one MVG.

The inflow conditions are generated using the following steps:

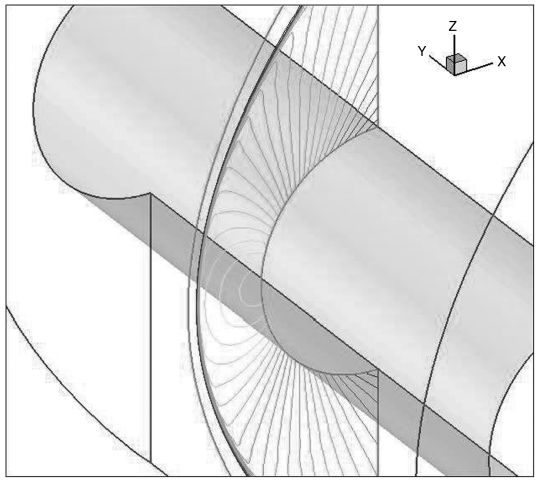

Fig. 1 Isobar contour of the pressure.

1) A turbulent mean profile is obtained from [10] about the streamwise velocity and the distribution is scaled using the local displacement thickness and freestream velocity.

2) The pressure is uniform at the inlet, which is specified as the freestream value. The temperature profile is obtained using Walz's equation for the adiabatic wall:

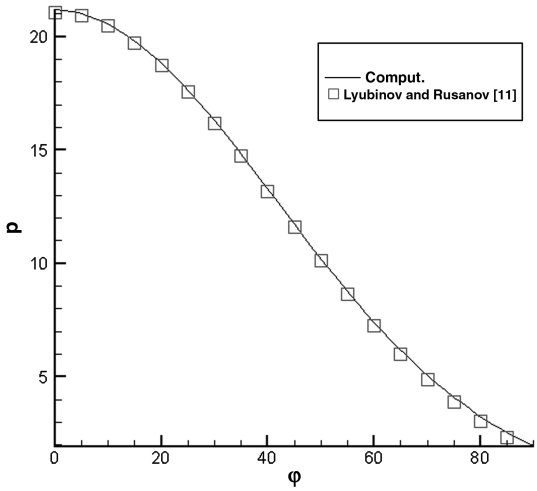

Fig. 2 Comparison of the pressure distribution with that of Lyubinov and Rusanov [11].

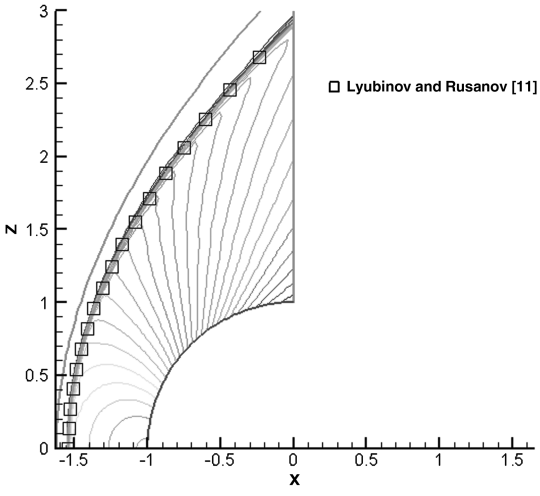

Fig. 3 Comparison of the shock location with that of Lyubinov and Rusanov [11].

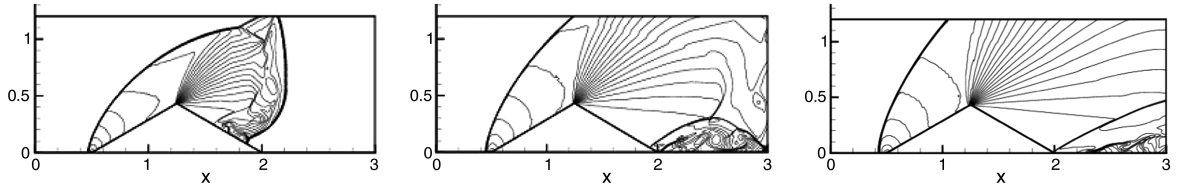

Fig. 4 Isodensity contour at different times.

a) First, the adiabatic wall temperature is determined using $T_w = T_e(1 + r(\gamma - 1)/2 \times M_e^2)$, where the subscript e means the edge of the boundary layer and r is the recovery factor with value 0.85.

b) The temperature profile is obtained by Walz's equation: $T/T_e = T_w/T_e - r(\gamma - 1)/2 \times M_e^2(U/U_e)^2$.

3) Random fluctuations are added on the primitive variables: i.e., u, v, w, p, and ρ. The disturbance has the form: $\varepsilon_{\text{distb}} e^{-(y-y_w)^2/\Delta y_{\text{distb}}} \times (\text{random} - 0.5)/2$, where the subscript distb means the disturbance and random is the random function with a value between 0–1, $\varepsilon_{\text{distb}}$ equals 0.1, and Δy_{distb} equals $2/3\delta$.

Such inflow conditions are, of course, not the exact solutions of the Navier–Stokes equations. The flow solver will adjust and modulate the flow into a weakly turbulent one while propagating downstream. More information will be given in Sec. IV.

C. Code Validation

Two validating tests are made as follows.

The supersonic inviscid flow is tested around the half-cylinder at $M_\infty = 4$. Because the fifth-order WENO scheme is a quite matured method and the problem studied in the paper contains shock waves, a validating test with a half-cylinder is selected to test the correctness of the code system.

Figure 1 shows the isobar contour in the middle section, which indicates that the scheme can capture the shock wave without visible oscillations. Figures 2 and 3 show the comparison between the numerical results and the asymptotic solution by Lyubinov and Rusanov [11], which is usually considered as the theoretical solution of that problem. A good agreement has been obtained between the two results.

The inviscid moving shock wave is tested passing over a sharp wedge. To demonstrate the ability of the boundary processing methods for the open-boundary, a numerical example is designed for a moving shock passing over a delta wedge. The Mach number of the incoming flow is 1.8 or the shock-wave Mach number is 8.293. The length and width of the domain are 3 and 1.2, and the angle of the wedge is 30°, which starts from 0.5 to 2 in the horizontal direction. The left, upper, and right boundaries are all treated as open boundaries in computation. Figure 4 shows three moments of the unsteady flow. The results indicate that the presented boundary processing methods can handle the boundary flow even with strong moving shock waves, and no distinct reflections are observed around the upper boundary.

III. Grid Generation

To study the effect of the declining angles of the trailing edge, two MVG cases are designed with two different angles: i.e., 45 and 70°. The apexes of the MVGs are placed at the same location. The technology of body-fitted grids is adopted in order to preserve the accuracy of the geometry and reduce numerical errors as much as possible while using a fifth-order WENO scheme. According to our experience, body-fitted grids are very important to the high resolution of the flow structure.

The geometries for the two cases are shown in Figs. 5 and 6. Except for the declining angle, other geometric parameters in the figures are the same as those given by Babinsky et al. [4]: i.e., $c = 7.2h$, $\alpha = 24°$, and $s = 7.5h$. In this study, the height of the MVG h is assumed to be $\delta_0/2$, where δ_0 is the inflow nominal boundary-layer thickness. MVGs are mounted on flat plates as in the experiments. For case 1, the horizontal distance from the apex of the MVG to the end of the plate is $33.7092h$; the distance for the case 2 is $34.3414h$. For both cases, the height of the domain is $10h$ and the width of the half-domain is $3.75h$.

Because of the complexity of the MVG geometry, it is better to partition the domain into several parts to confine the singularity into a local region. As shown in Fig. 7, three regions are divided as the fore region, MVG region, and downstream region. Between each two regions, there is a grid transition buffer. Because of the symmetry,

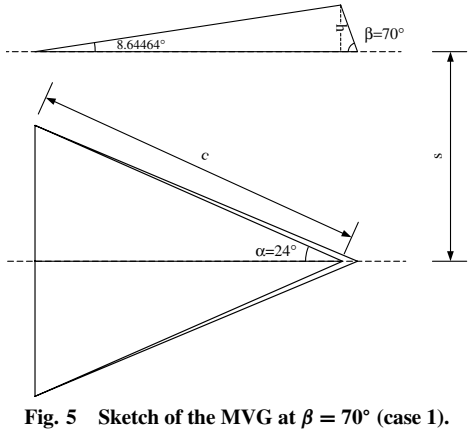

Fig. 5 Sketch of the MVG at $\beta = 70°$ (case 1).

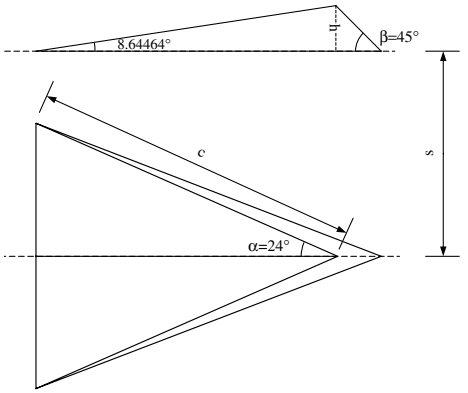

Fig. 6 Sketch of the MVG at $\beta = 45°$ (case 2).

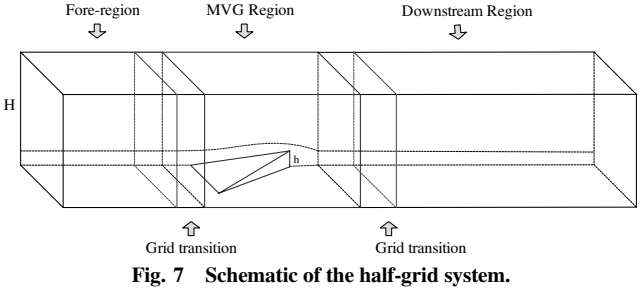

Fig. 7 Schematic of the half-grid system.

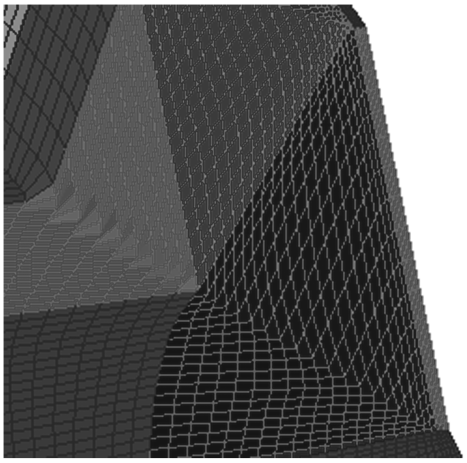

Fig. 8 Smoothness of the trailing edge for case 2.

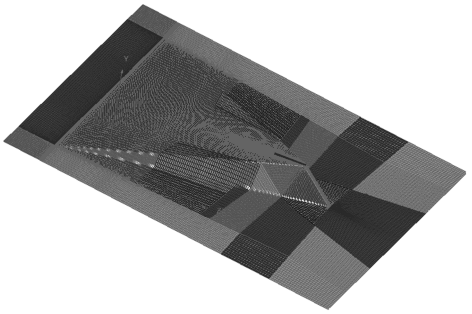

Fig. 9 Surface grids of the MVG in patches for case 2.

only half of the grids were generated. The grid number for the whole system is $n_{\text{spanwise}} \times n_{\text{normal}} \times n_{\text{streamwise}} = 128 \times 192 \times 1600$.

Taking case 2 as an example, the following steps are adopted to generate the grids:

1) The downstream region is generated separately, which can later provide a reference for the volume grid generation of the MVG region. In the normal direction, grid clustering is carried out to locate half of the grids under the height 1.2δ or $2.4h$, but uniform grids are used in other directions of the grid frames. Simple transfinite interpolation method is used to generate the 3-D volume grids.

2) To generate the complete grids of the MVG, it is essential to generate a surface grid first. The quality of the surface grids will directly influence the quality of the 3-D volume grids. An accurate description of the geometry by surface grids will enhance the accuracy of the computation. Because the surface of the MVG is of high singularity, it failed to use the automatic grid-generation technique such as projection by some commercial software. In the study, manual adjustment is used by the following steps. First, a modification is made by smoothing the trailing edge using a very small arc (Fig. 8). Next, the surface is divided into many small patches, and so the singularity of the shape is reduced in each patch.

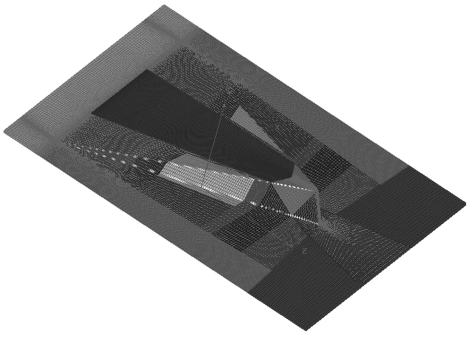

Fig. 10 Surface grids of the MVG in patches for case 1.

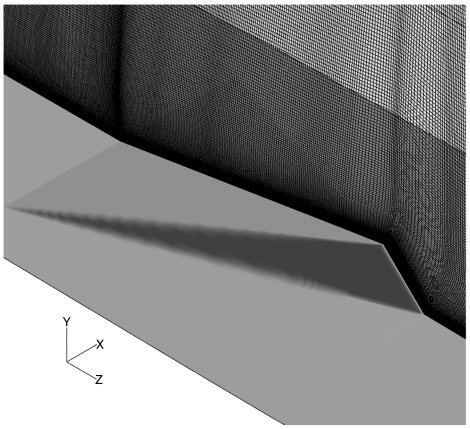

Fig. 11 MVG and grids at central plane.

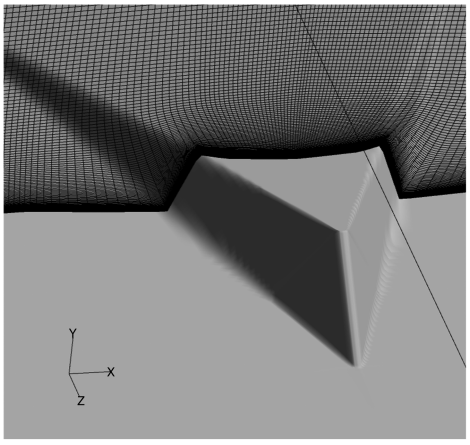

Fig. 12 Grids in certain cross sections.

Third, the skeleton grid lines are constructed manually in the patch using some software in an interactive manner. Afterward, the lines are discretized into grid points. Careful adjustments are made to make the distribution of grids as smooth as possible. Finally, optimization is made to let grid lines transit smoothly among patches. The final surface grids can be found in Fig. 9. For comparison, the surface grid for case 1 is shown in Fig. 10.

3) The connection of grids of the MVG and downstream regions is made afterward. Using the beginning section of the downstream grids as a reference, the frame grid lines of the MVG region can be determined. Using some software, it is easy to generate the other surface grids. Special orthogonal procedures are taken on the central

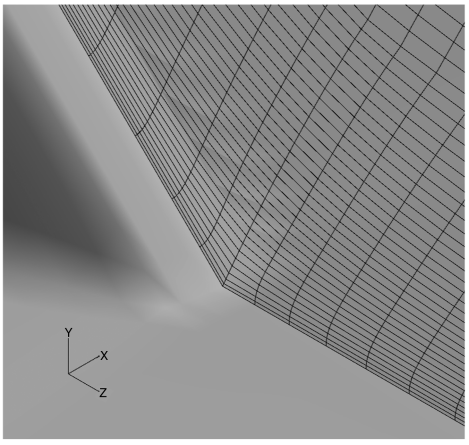

Fig. 13 Grids at the foot of the trailing edge.

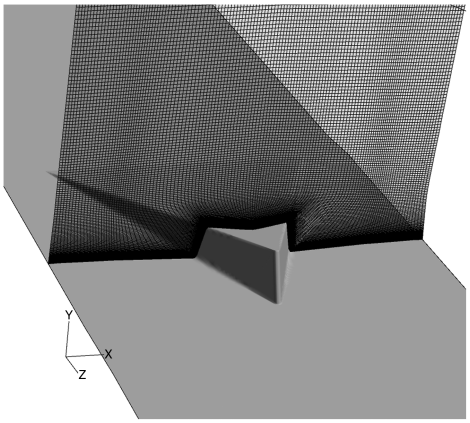

Fig. 14 Grids in cross section 1.

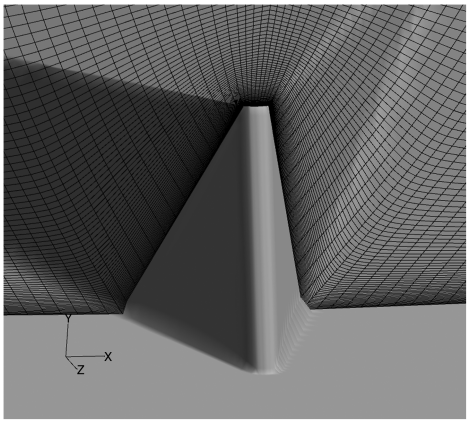

Fig. 15 Grids in cross section 2.

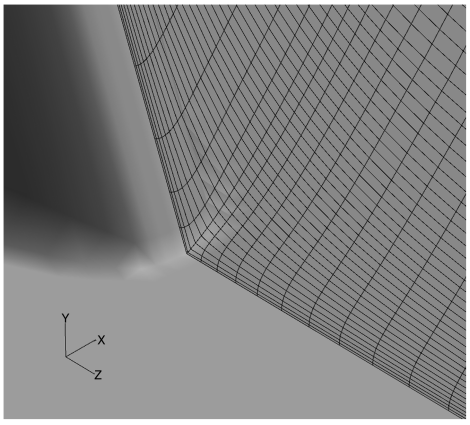

Fig. 16 Grids at the foot of the trailing edge.

symmetric grid plane. After all surface grids are generated, the 3-D volume grids are constructed using transfinite interpolation.

Further optimization on grids is conducted to make the volume grids more orthogonal to the body surface and smoothly change in space. The method is to run the elliptic grid-generation solver several times, while making sure that there is no additional distortion introduced in each run. After that, a grid transition zone is divided from the downstream region. The grids in that zone are redistributed to make the mesh transition continuous from the MVG region to the downstream region.

4) Using the beginning section of the MVG grid, the frame grid lines of the fore region can be determined. Transfinite interpolation method is used to generate the 3-D volume grids. After that, a grid transition zone is divided again from the fore region. The grids in that region are redistributed to make the mesh transition continuous from the MVG region to the ramp region.

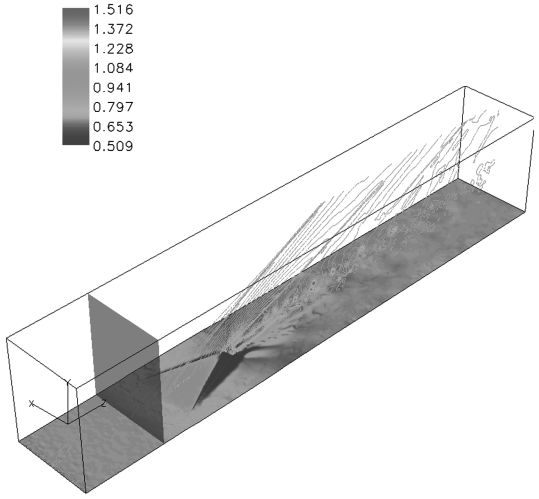

Fig. 17 Location of the section for checking.

The final grids can be seen in Figs. 11–13. Using the parameters from the mean flow profile, the length of the first grid interval at the entrance section is found to be around 0.93 in wall unit ($y^+ = 0.93$).

The procedures for case 1 are similar for case 2. The generated grids are demonstrated in Figs. 14–16.

IV. Computational Results

A. Inflow Boundary-Layer Profiles

The flow profiles are checked ahead of the MVG after long periods of computation. To define a reference coordinate system in this and the following sections, the apex of the MVG is selected as the original point. The section for checking is located at $z = -10.3775h$, which is illustrated in Fig. 17. At this section, the pitot pressure recovery coefficient and H_i are calculated and averaged in the spanwise direction. The pitot pressure recovery coefficient used in this work is defined as

$$C_{\text{pitot}_{\text{rc}}} = \frac{1}{H}\int_0^H \frac{p_0}{p_{0\infty}}\,\mathrm{d}y \tag{17}$$

where H can be of a value near the height of the domain. The averaged $C_{\text{pitot}_{\text{rc}}}$ is 0.940676, and the averaged H_i is 1.928393. As is well known, H_i for the laminar flow is around 2.6 and for the standard turbulent flow is about 1.2–1.4. So the results indicate that the methods described in Sec. II.B.5 produce a kind of weakly turbulent flow.

B. Comparative Study on the Flow of the MVG at $\beta = 70$ and 45°

In [12], computations and detailed analyses have been made on the MVG-controlled (at $\beta = 70°$) ramp flow at the same inflow condition. The geometry [12] in front of the ramp is the same as that in case 1, and the geometry [12] in front of the MVG is the same as that in case 2. Therefore, only a brief introduction will be given about the common features of the two cases. More information can be found in [12].

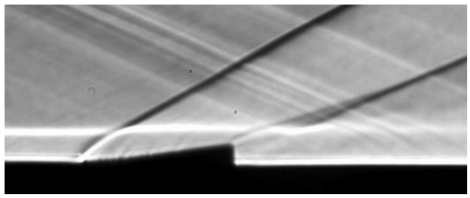

Fig. 18 Schlieren photograph from Babinsky et al. [4].

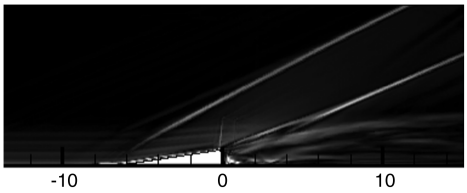

Fig. 19 Digital schlieren of case 1 ($\beta = 70°$).

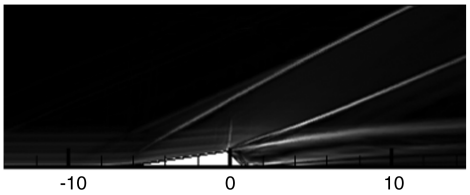

Fig. 20 Digital schlieren of case 2 ($\beta = 45°$).

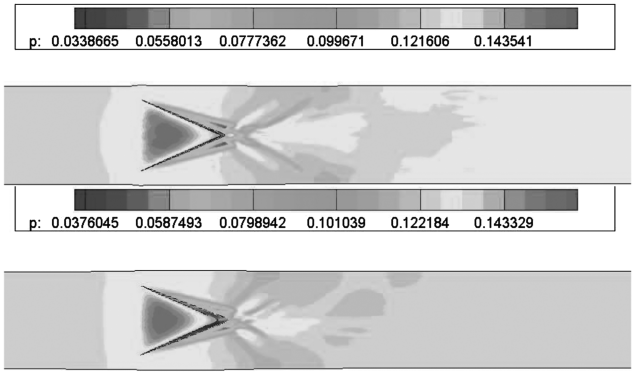

Fig. 21 Surface pressure contour of case 1 (upper) and case 2 (down).

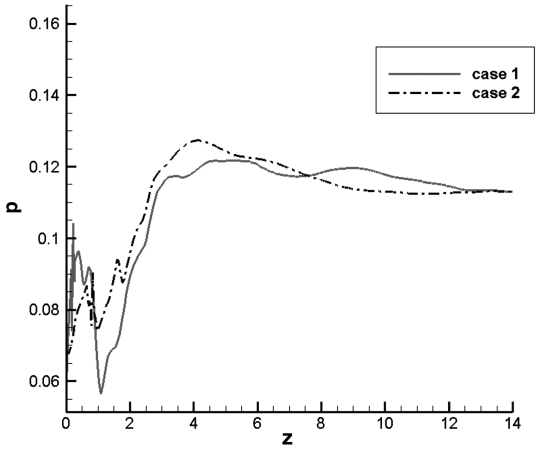

Fig. 22 Surface pressure distribution of two cases from the apex of the MVG at the central line.

1. Common Features

As indicated by Babinsky et al. [4], the structure of the wave system of the MVG flow consists of the first reflection shock, the expansion wave system, and the recompression shock (see Fig. 18). According to results in [12], the recompression shock waves make the flow satisfy the virtual boundary conditions generated by the streamwise vortices. Moreover, the recompression shock has the arclike 3-D structure. The structure of the surface pressure is characterized by a pair of oblique high-pressure slots after the MVG, which are followed by a pair of low-pressure expansion slots.

The surface separation pattern is characterized by a pair of primary separations, which correspond to the primary counter-rotating streamwise vortices, and by two pairs of secondary separation on the side of the MVG and beside MVG. The primary separations end in a degenerate nodal point related to limiting streamlines, but the secondary separations end in spiral points; after that, a new pair of secondary separations are generated. About the 3-D spatial structures of the vortices, primary and secondary streamwise vortices can be shown by cross-sectional streamlines. The intensity of vortices is reduced when moving downstream.

The specific streamwise momentum deficit phenomenon exists after the flow passes the MVG. The shape of the deficit is a circlelike region when shown at the spanwise cross section. According to [12], the main source of the deficit comes from the shedding of the upstream boundary layer from the MVG. Along with entrainment of the streamwise vortices, some low-momentum fluid from the boundary layer might be added to the deficit by the upwash effect.

The deficit will produce a high shear layer around its boundary. The shear layer will lose the instability due to the mechanism of the Kelvin–Helmholtz instability. Vortex rings are then generated within the shear layer and strongly interact with the flow.

2. Comparison of the Flow Structures in Two Cases

a. Wave Structures. In Figs. 19 and 20, the numerical schlieren of the time-averaged computation results in the two cases are given at the central plane, which uses the time-averaged density of the flow. For comparison, the photograph from Babinsky et al. [4] is shown in Fig. 18. The oblique λ structure is more obvious in case 1 than in case 2. The angles for the first shock are almost the same: i.e., 26.9°. The angles for the recompression shock are different: 21.93° for Babinsky, 24.66° for case 1, and 23.36° for case 2.

The surface pressure is different between the two cases. In case 1, there is an isolated high-pressure spot behind the MVG and the length of the oblique high-pressure slot is longer than that of case 2, as shown in Fig. 21. Figure 22 gives the comparison of the time-averaged pressure distribution along the central line. The location at $z = 0$ corresponds to the apex of the MVG. The results indicate that there exists stronger compression and higher pressure rise in the region after the end of the MVG in case 1 than that in case 2.

b. Separation Patterns. Comparisons are made on the surface separation first. Figure 23 shows the surface separation of case 1 (top) and case 2 (bottom). Although there is less topology difference from the top view, the side views show that the secondary separation on the side of the MVG in case 2 is smaller and less obvious than that of case 1, and the positions are also different.

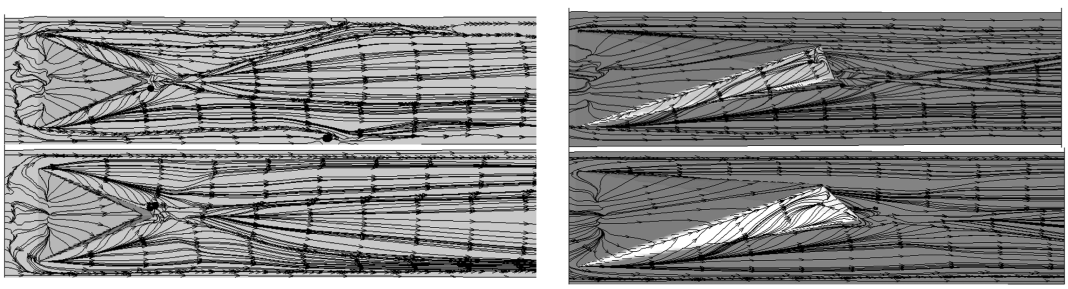

a) Top view **b) Side view**

Fig. 23 Surface separation of case 1 (upper) and case 2 (down).

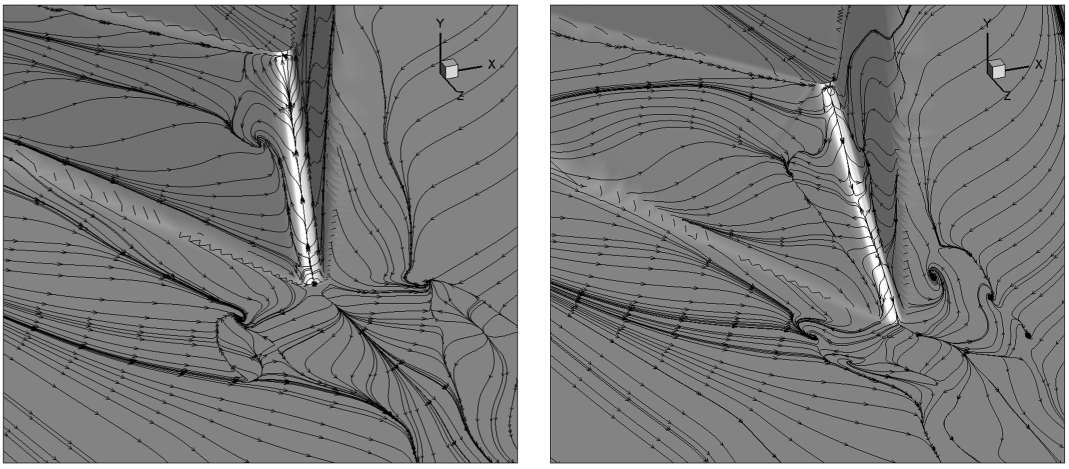

a) Case 1 b) Case 2

Fig. 24 Surface separation pattern around the trailing edge of the MVG.

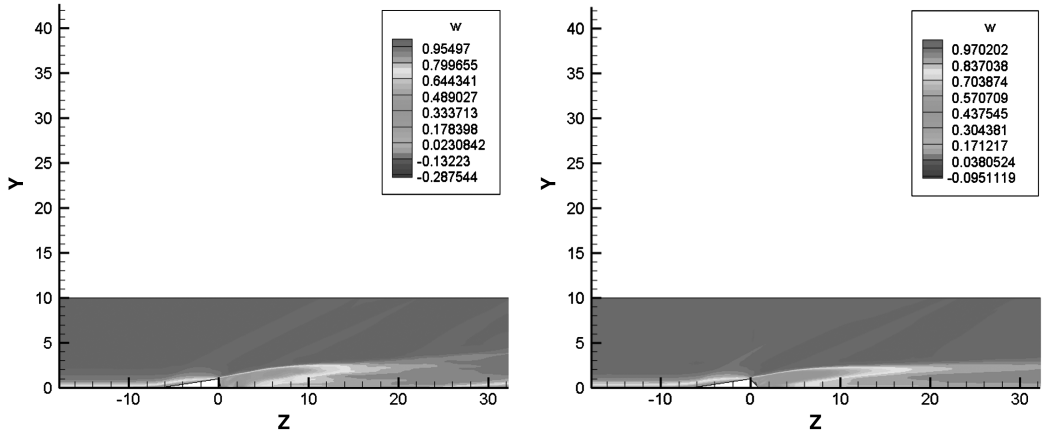

Fig. 25 Momentum deficit of the MVG for case 1 (left) and case 2 (right) at the center plane.

To further investigate the difference, the local views of the two cases are given in Fig. 24 around the trailing edge. The figure shows that the start of the secondary separation after the MVG in case 2 is of the compound type, and the secondary separation on the side of the MVG ends in a degenerate nodal point, not the spiral point as found in case 1. The separation at the foot of the trailing edge of the MVG in case 2 is more complex than that in case 1.

For the spatial structures of the streamwise vortices, the cross-sectional separation patterns are checked on several spanwise sections. The difference between the two cases is that the streamwise vortices are located lower in case 2 than in case 1. This feature will be further checked in the following sections. The shape and position of the vortices are different, but the topology seems to be similar.

c. Momentum Deficit. In Fig. 25, the momentum deficit is given at the central plane using the averaged streamwise velocity (w velocity). The figure shows that the trajectory of the deficit in case 2 is lower than that of case 1, and the existence of the deficit in case 2 also lasts longer. Because the momentum deficit is closely related to the vortex development, the result implies that the vortices in case 2 stay closer to the wall and might last longer.

In Fig. 26, the time-averaged Mach number contour is given at the central plane. The results show that there is a larger subsonic region

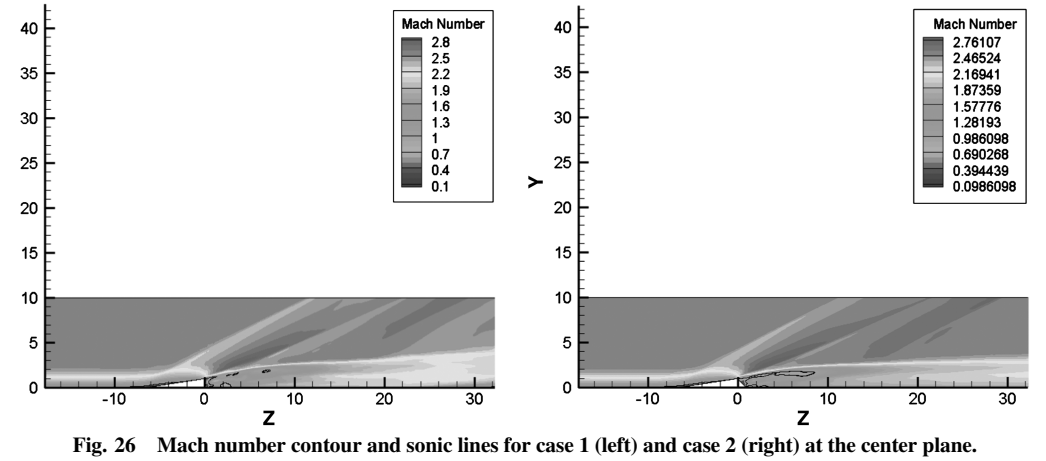

Fig. 26 Mach number contour and sonic lines for case 1 (left) and case 2 (right) at the center plane.

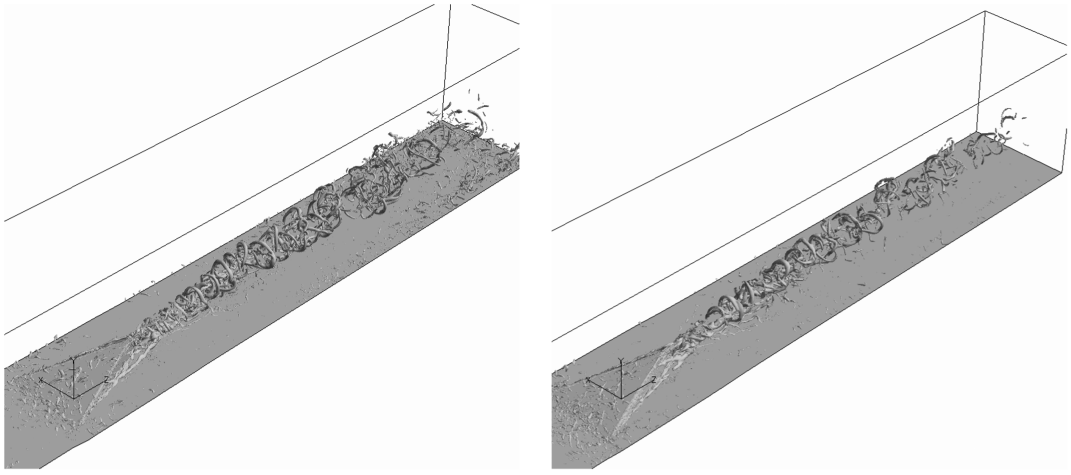

Fig. 27 Isosurface of λ_2 for case 1 (left) and case 2 (right).

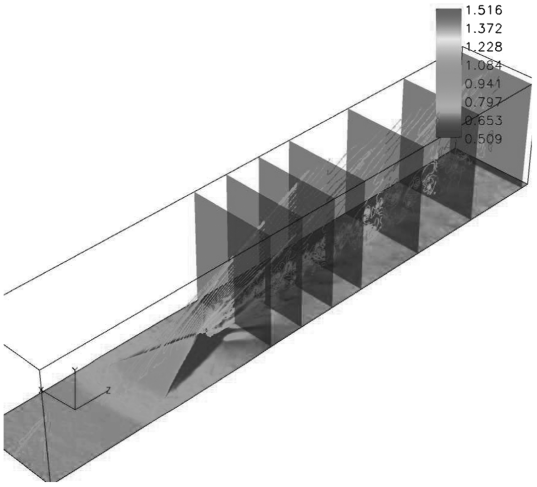

Fig. 28 Location of sections for checking.

after MVG in case 1. Moreover, a subsonic region is observed on the wall. Such a distribution indicates the deceleration of the boundary-layer flow and is apt to lift up the streamwise vortices; therefore, it is unfavorable to flow control. However, there is a subsonic region in the outer region of the boundary layer in case 2, which is favorable to the maintenance of the vortices; meanwhile, the subsonic region also means the shear layer produced by the momentum deficit has the stronger intensity.

d. Vortex Rings. In Fig. 27, the instantaneous images are drawn using the isosurface of λ_2 [13], which is the second eigenvalue of the 3×3 matrix composed of a velocity gradient, i.e., $M_{ij} = \sum_{k=1}^{3}(\Omega_{ik}\Omega_{kj} + S_{ik}S_{kj})$, where $\Omega_{ij} = 1/2(\partial u_i/\partial x_j + \partial u_j/\partial x_i)$, and $S_{ij} = 1/2(\partial u_i/\partial x_j - \partial u_j/\partial x_i)$. A small negative value is selected for visualization. From the figures, no structural difference is observed between two cases.

To get the quantitative information about the location of the chain of the vortex rings, the numerical schlieren image in Figs. 19 and 20 is used to determine the height corresponding to the upper edge of rings at exit. The measured height is $4.06936h$ for case 1 and $3.3881h$ for case 2. The results confirm the conclusion in the previous section; i.e., the vortices in case 2 stay closer to the wall.

3. Comparison of the Quality of Downstream Boundary Layer

Using the same method in Eq. (17), the spanwise-averaged incompressible displacement thickness, momentum thickness, shape factor and the pitot pressure recovery coefficient are calculated based on the time-averaged data at certain downstream section. The streamwise distance of the section to the apex of the MVG is $26.66h$. The results for case 1 are that the incompressible displacement thickness is $0.221126h$, the incompressible momentum thickness is $0.1408h$, the shape factor H_i is 1.6725, and the pitot pressure recovery coefficient is 0.93595. For case 2, the incompressible displacement thickness is $0.2070689h$, the incompressible momentum thickness is $0.131697h$, the shape factor H_i is 1.63877, and the pitot pressure recovery coefficient is 0.92388. The differences between the two cases are not obvious.

4. Discussion About the Mechanism of the Difference Resulted By Different Declining Angles

From the above sections, it can be found that the declining angle of the MVG at $\beta = 45°$ will result in the lower position of the

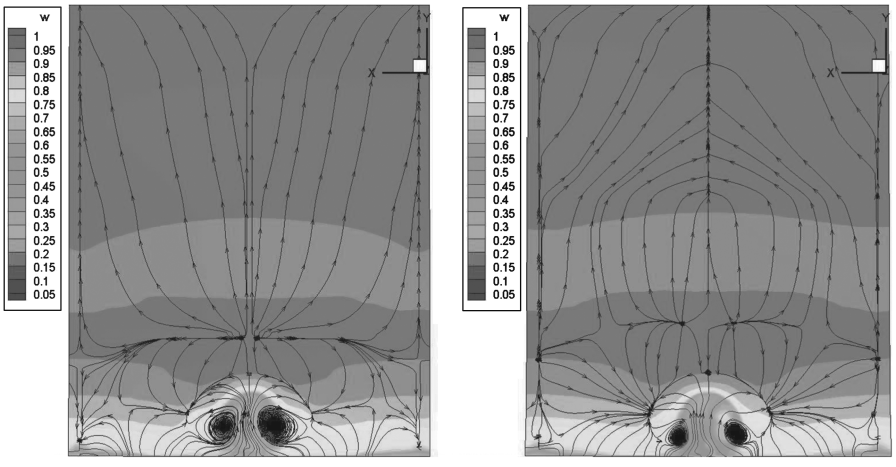

Fig. 29 Cross-sectional streamlines for case 1 (left) and case 2 (right).

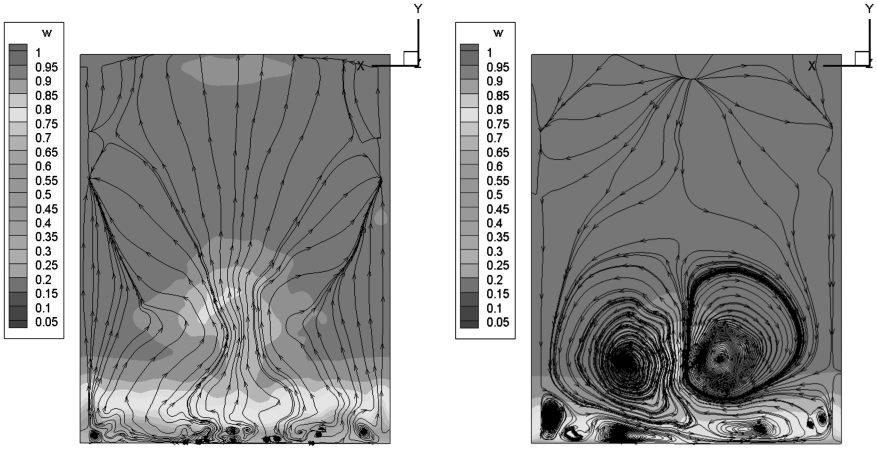

Fig. 30 Cross-sectional streamlines for case 1 (left) and case 2 (right).

streamwise vortices and the corresponding vortex rings. The possible reasons might be as follows:

1) There is a larger dead-water region at the trailing edge of the MVG at $\beta = 70°$, which will cause a stronger adverse pressure gradient and make the vortex lift up.

2) The larger declining angle makes the end of the MVG wider and therefore makes the streamwise vortices separate from each other, which alleviates the upwash effect in the end.

To illustrate this, the cross-sectional streamlines are drawn and investigated at certain spanwise sections as shown in Fig. 28. The sections are approximately located in the same streamwise distance to the apex of the MVG for two cases. In Fig. 29, the streamlines are displayed in the first section in Fig. 28. It can be seen that the vortices in case 2 are more separated from each other and stay lower to the wall.

In Fig. 30, an additional check of the streamwise vortices is shown in the last section in Fig. 28. It can be seen that for case 1, the streamwise vortices largely degenerate and are hardly observable; for case 2, the vortices still exist, even if they might not be strong. This result validates the former conclusion once more; i.e., the streamwise vortices in case 2 stay closer to the wall and last longer in the downstream region.

V. Conclusions

Using the MILES method and fifth-order WENO scheme, comparative studies are made on the MVG flow at $M = 2.5$ and $Re_\theta = 1440$. The MVGs are designed with different declining angles, i.e., $\beta = 70$ and 45°, to study the declining effect. The body-fitted grid scheme is adopted to ensure that the computations have high accuracy. The following conclusions can be made:

1) The basic structures are similar in two cases, such as the wave system, separation pattern, momentum deficit, vortex rings, etc. The effect of declining angle does not bring out the structural difference, while differences exist in the details of the flow.

2) The smaller declining angle at $\beta = 45°$ makes the vortices closer to the wall, which include the initial streamwise vortices and the following series of vortex rings. This should be more favorable to flow control. Nevertheless, the quantitative analyses on the time-averaged data at a downstream section do not exhibit a significant improvement in the quality of the boundary layer.

Acknowledgments

This work is supported by U.S. Air Force Office of Scientific Research grant FA9550-08-1-0201, supervised by John Schmisseur. The authors are grateful to Texas Advantage Computing Center for providing computation hours.

References

[1] Ashill, P. R., Fulker, J. L., and Hackett, K. C., "Research at DERA on Sub Boundary Layer Vortex Generators (SBVGs)," AIAA Paper 2001-0887, 2001.

[2] Ashill, P. R., Fulker, J. L., and Hackett, K. C., "A Review of Recent Developments in Flow Control," *The Aeronautical Journal*, Vol. 109, No. 1095, 2005, pp. 205–232.

[3] Anderson, B. H., Tinapple, J., and Surber, L., "Optimal Control of Shock Wave Turbulent Boundary Layer Interaction Using Micro-Array Actuation," AIAA Paper 2006-3197, 2006.

[4] Babinsky, H., Li, Y., and Pitt Ford, C. W., "Microramp Control of Supersonic Oblique Shock-Wave/Boundary-Layer Interactions," *AIAA Journal*, Vol. 47, No. 3, 2009, pp. 668–675. doi:10.2514/1.38022

[5] Lee, S., and Loth, E., "Supersonic Boundary Layer Interactions with Various Micro-Vortex Generator Geometries," AIAA Paper 2009-3712, 2009.

[6] Urbin, G., Knight, D., and Zheltovodov, A. A., "Compressible Large-Eddy Simulation Using Unstructured Grid: Supersonic Turbulent Boundary Layer and Compression Corner," AIAA Paper 99-0427, 1999.

[7] Jiang, G., and Shu, C. W., "Efficient Implementation of Weighted ENO Schemes," *Journal of Computational Physics*, Vol. 126, 1996, pp. 202–228. doi:10.1006/jcph.1996.0130

[8] Shu, C. W., and Osher, S., "Efficient Implementation of Essentially Non-Oscillatory Shock-Capturing Schemes," *Journal of Computational Physics*, Vol. 77, 1988, pp. 439–471. doi:10.1016/0021-9991(88)90177-5

[9] Li, Q., Zhang, H., and Gao, S., "An Hybrid Fourth Order Scheme, Boundary Condition Based on Characteristic and Their Applications," *Acta Aerodynamica Sinica*, Vol. 18, No. 2, 2000, pp. 146–155.

[10] Liu, C., and Chen, L., "Study of Mechanism of Ring-Like Vortex Formation in Late Flow Transition," AIAA Paper 2010-1456.

[11] Lyubinov, A. N., and Rusanov, V. V., "Gas Flow past Blunt Bodies," NASA TT-F715, 1973.

[12] Li, Q., and Liu, C., "LES for Supersonic Ramp Control Flow Using MVG at $M = 2.5$ and $Re_\theta = 1440$," AIAA Paper 2010-592, 2010.

[13] Tufo, H. M., Fischer, P. F., Papka, M. E., and Blom, K., "Numerical Simulation and Immersive Visualization of Hairpin Vortices," *Proceedings of the 1999 ACM/IEEE Conference on Supercomputing* [CD-ROM], Association for Computing Machinery, New York, 1999, Paper 62.